Research Square

Preprints are preliminary reports that have not undergone peer review.
They should not be considered conclusive, used to inform clinical practice,
or referenced by the media as validated information.

Fast Spotlight SAR Raw Data Generation via Error-Constrained Local Coherent Equivalence

Jiawei Liu[1]
Beijing Institute of Radio Metrology and Measurement
Lei Zhao[1]
Beijing Institute of Radio Metrology and Measurement
Xuesheng Chu[1]
Beijing Institute of Radio Metrology and Measurement
Tiezeng Jiang[1]
Beijing Institute of Radio Metrology and Measurement
Chuang Li[1]
dlyanlc@163.com
Beijing Institute of Radio Metrology and Measurement
Shuyong Zhou[1]
Beijing Institute of Radio Metrology and Measurement

Research Article

Keywords: spotlight SAR, SAR raw data generation, phase-error constraint, local coherent equivalence, reuse of key pulse, frequency-domain sparse convolution

Posted Date: November 16th, 2026

DOI: https://doi.org/10.21203/rs.3.rs-11356730/v1

License: This work is licensed under a Creative Commons Attribution 4.0 International License.
Read Full License

Additional Declarations: No competing interests reported.

Fast Spotlight SAR Raw Data Generation via Error-Constrained Local Coherent Equivalence

Jiawei Liu[1], Lei Zhao[1], Xuesheng Chu[1], Tiezeng Jiang[1], Chuang Li[1]*, Shuyong Zhou[1]

[1]Beijing Institute of Radio Metrology and Measurement, No. 50 Yongding Road, Haidian District, Beijing, China

*Corresponding author: dlyanlc@163.com

Abstract

Fast phase-consistent raw data generation supports spotlight synthetic aperture radar (SAR) system design and evaluation, but simulating complex three-dimensional targets remains computationally demanding. This study presents an error-constrained local coherent equivalence method within a frequency-domain sparse-convolution framework. In each platform-state update interval, selected key pulses are used to form phase-calibrated equivalent complex amplitudes for local scattering-center groups. These amplitudes are reused at assigned non-key pulses while the representative-point delay, carrier phase, visibility, and amplitude are updated. A unified propagation-phase model distinguishes inter-pulse carrier-phase deviation from baseband spectral-phase deviation; relative range-history screening, range-support and coherence criteria, and pointwise fallback govern the approximations. For a three-dimensional ship scattering-center model, the method achieved online speedups of 3.028–3.114 over the full frequency-domain baseline across four broadside trajectories. Relative to the direct time-domain reference for each case, its complex raw-echo and back-projection (BP) image normalized root-mean-square errors (NRMSEs) were approximately 0.061 and 0.053, compared with 0.0135 and 0.0043 for the frequency-domain baseline. In the single 15° forward-squint case, the online speedup was 2.719, with raw-echo and BP-image NRMSEs of 0.0440 and 0.0381. These results quantify the online speed–fidelity trade-off for the tested target and geometries.

Keywords: spotlight SAR, SAR raw data generation, phase-error constraint, local coherent equivalence, reuse of key pulse, frequency-domain sparse convolution

1 Introduction

Synthetic aperture radar (SAR) raw data generation provides a controlled means of evaluating radar configurations and image-formation algorithms [1,2]. SAR systems operate in several imaging modes, including stripmap, ScanSAR, and spotlight [3]. In spotlight mode, the antenna beam is steered toward the same target area throughout the synthetic aperture, enabling sustained coherent observation and high azimuth resolution [2]. The changing viewing aspect over this aperture also makes spotlight SAR relevant to the high-resolution imaging of complex targets.

Raw data generation methods are commonly classified as time-domain, frequency-domain, and hybrid approaches. Direct time-domain generation sums pulse-wise scattering contributions with their geometry-dependent delays and carrier phases [4,5]. To reduce the repeated phase computation for scenes containing three-dimensional targets, Dogan and Kartal reuse a precomputed oversampled waveform [6]. Frequency-domain methods, in contrast, accelerate the generation of spotlight raw data for extended scenes through spectral processing [2]. Subsequent formulations extend this spectral approach through coordinate transformations, spectral interpolation, and curvilinear integration [7-11]. Hybrid methods combine frequency-domain processing with time-domain integration or phase evaluation [3,12]. These approaches improve waveform synthesis and accommodate diverse geometries. However, methods that form a per-pulse response from densely distributed three-dimensional scattering centers still require repeated coherent assembly and repeated updates of complex-valued weights, and their cost grows with the number of scattering centers and pulses.

Subaperture processing has been used to reduce SAR raw data generation time for extended scenes by exploiting similarities among neighboring pulses [13]. Wen and Zeng further grouped pulses and divided the scene into range rings and rectangular subscenes, thereby constructing group transfer functions more efficiently [14]. Echoes from complex targets

can be represented as sums of discrete scattering-center contributions [15]. More generally, once an echo is expressed as a sum of discrete contributions, combining them into equivalent responses makes it possible to accelerate raw data generation. Closer to the proposed work, the scatterers within each equidistant range ring were aggregated into one equivalent response and combined with subaperture and polar-subscene processing [16]. The same framework was subsequently extended to one-stationary bistatic SAR using elliptical range rings and derived the bound that the phase error places on the subaperture length [17]. These studies already combine spatial equivalence and aperture grouping, yet their range-ring formulations leave unspecified how the scattering centers of a pre-established three-dimensional target should be grouped so that pulse-dependent visibility and aspect responses are retained. For this target representation, the remaining question is how to jointly select local coherent groups that preserve pulse-dependent visibility and aspect responses and the key-pulse reuse intervals, and how to control the phase deviations introduced by both spatial delay approximation and inter-pulse evolution.

Reducing these costs requires two approximations with different phase consequences. Spatially combining several scattering centers under one selected delay perturbs the baseband spectral phase, whereas reusing an equivalent complex amplitude across neighboring pulses introduces a carrier-phase deviation as the relative ranges evolve. Treating either approximation independently does not specify how their errors should be controlled when local grouping, visibility, and reuse intervals interact. A remaining need is therefore a unified propagation-phase deviation model that links the slant-range span of each local group to the reuse interval over which its equivalent complex amplitude is reused.

To meet this need, we propose a fast raw-data generation method for monostatic spotlight SAR that combines error-constrained local coherent equivalence and key-pulse reuse using a pre-established three-dimensional scattering-center model and prescribed platform trajectories. The unified propagation-phase deviation model separately constrains the baseband spectral-phase deviation introduced by substituting the representative center’s

delay and the inter-pulse carrier-phase deviation introduced by the reuse of equivalent complex amplitude. Scattering centers with similar relative range histories are organized into local groups of limited slant-range span, each represented by an actual scattering center, while contributions that fail the coherence or visibility conditions retain separate responses. Equivalent complex amplitudes are constructed at selected key pulses for groups screened by sampled relative range-history checks and reused at assigned non-key pulses within the corresponding reuse intervals. At each pulse, the representative center supplies the current propagation delay and carrier phase. The resulting sparse impulse response reduces both the number of response entries and the frequency of complex-amplitude reconstruction before frequency-domain raw-data synthesis. We evaluate the method in terms of computational speed and imaging accuracy.

2 Materials and Methods

This section formulates the monostatic spotlight SAR raw echo and the frequency-domain sparse-convolution baseline. It then derives the propagation-phase deviation model, the relative range-history grouping, the coherent equivalence at key pulses, the inter-pulse reuse rule, and the resulting equivalent sparse impulse response. The final subsections describe the scattering-center input, back projection (BP) validation, and experimental configuration.

2.1 Monostatic Spotlight SAR Geometry and Time-Domain Raw Echo Model

Consider a monostatic spotlight SAR platform whose beam tracks a target throughout the synthetic aperture. Let $\boldsymbol{p}_m$ denote the three-dimensional radar phase-center position at the mth pulse, and let $\boldsymbol{q}_n$ denote the position of the nth scattering center. The instantaneous monostatic slant range is

$$R_{n,m} = \|\boldsymbol{p}_m - \boldsymbol{q}_n\|_2 \tag{1}$$

The aperture-center squint angle θ_{sq} is measured in the horizontal plane between the projected line of sight and the broadside direction perpendicular to the platform velocity; thus, $\theta_{sq} = 0°$ denotes broadside acquisition. The incidence angle θ_i is measured between the line of sight and the reference-plane normal. Figure 1 illustrates the observation geometry, platform trajectory, instantaneous slant range, squint angle, and incidence angle.

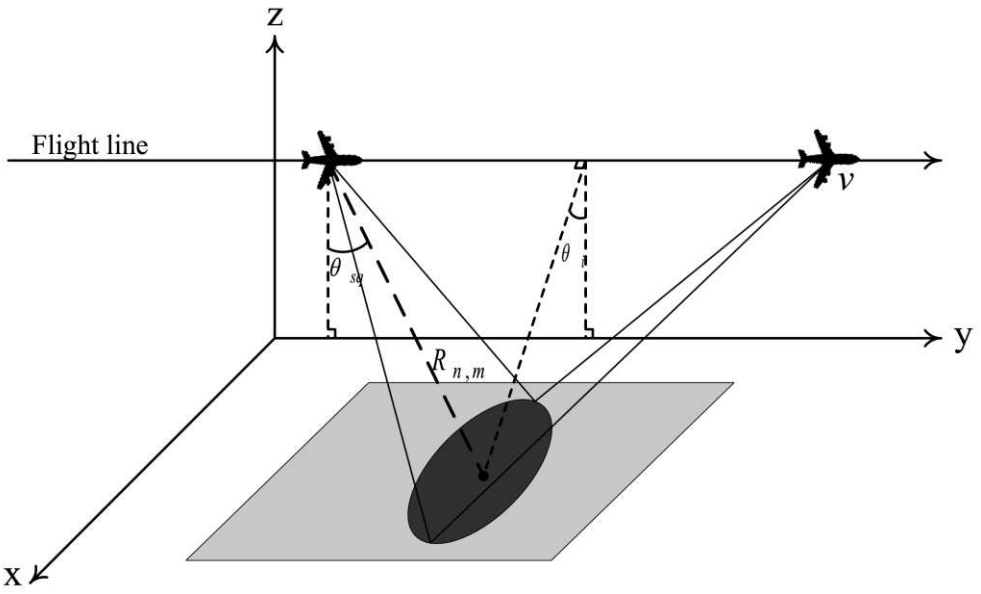


Fig. 1 Three-dimensional monostatic broadside spotlight SAR geometry.

For a transmitted linear frequency-modulated pulse $p(\tau) = \mathrm{rect}(\tau/T_p)\exp(j\pi K_r \tau^2)$, the time-domain raw echo at the mth pulse is

$$s_m(\tau) = \sum_{n\in I_m} \mathrm{rect}\left(\frac{\tau - 2R_{n,m}/c}{T_p}\right) \times \exp\left[j\pi K_r\left(\tau - \frac{2R_{n,m}}{c}\right)^2\right] a_{n,m}\exp\left(-j\frac{4\pi R_{n,m}}{\lambda}\right), \tag{2}$$

where τ is continuous fast time; I_m is the set of visible scattering centers at this pulse; T_p is the pulse duration; c is the speed of light; $K_r = \frac{B}{T_p}$ is the chirp rate; B is the signal bandwidth; $a_{n,m}$ is the complex amplitude of the nth scattering center at this pulse,

including pulse-dependent visibility, aspect response, and deterministic range weighting; and λ is the carrier wavelength.

The time-domain method evaluates the geometric slant range, propagation delay, and coherent carrier phase for every scattering center at every pulse, then generates and coherently sums the corresponding delayed chirps on the fast-time grid [5]. By retaining the individual geometric delays and coherent phase relationships, it provides a numerical reference for accuracy assessment.

2.2 Frequency-Domain Sparse-Convolution Echo Model

Each scattering-center contribution in Eq. (2) can be regarded as a complex-weighted and propagation-delayed replica of the transmitted pulse. The contributions of all visible scattering centers at the mth pulse can therefore be assembled into the sparse impulse response

$$h_m(\tau) = \sum_{n\in I_m} a_{n,m} \exp\left(-j\frac{4\pi R_{n,m}}{\lambda}\right)\delta\left(\tau - \frac{2R_{n,m}}{c}\right). \tag{3}$$

The raw echo can then be written as

$$\begin{aligned} s_m(\tau) &= p(\tau) \otimes h_m(\tau) = \mathcal{F}^{-1}[S_m(f)] \\ S_m(f) &= P(f)H_m(f), \end{aligned} \tag{4}$$

where f is fast-time frequency; $S_m(f)$, $P(f)$, and $H_m(f)$ are the continuous Fourier transforms of $s_m(\tau)$, $p(\tau)$ and $h_m(\tau)$ with respect to τ ,respectively.

Using the impulse-shift property, the time-domain echo in Eq. (2) is recast into the convolution form in Eq. (4). Direct evaluation of Eq. (3) requires traversing all visible scattering centers at every pulse. Their complex amplitudes, propagation delays, and carrier phases are updated before the corresponding entries are written to the sparse impulse response. As the numbers of scattering centers and pulses increase, this scatterer-by-scatterer and pulse-by-pulse response construction becomes a major computational cost.

The total cost of the frequency-domain model is therefore determined not only by the fast Fourier transforms (FFTs) and frequency-domain multiplication, but also by the number of scattering centers and the frequency of their pulsewise updates. A viable route to further acceleration is to exploit local similarities among scattering contributions in both spatial distribution and slow-time evolution, so that the original sparse impulse response can be represented by fewer equivalent entries and fewer update operations under controlled approximation errors.

2.3 Error-Constrained Local Coherent Equivalence for Sparse Impulse Responses

A small subset of pulses is selected approximately uniformly within each platform-state update interval and designated as key pulses. The remaining pulses are treated as non-key pulses and assigned to their nearest key pulses in azimuth slow time. Inter-pulse reuse refers to the reuse, at associated non-key pulses, of an equivalent complex amplitude constructed at a key pulse. Under this organization, multiple scattering-center contributions in the sparse impulse response of Eq. (3) can be represented by a single phase-calibrated entry. Scattering centers with similar relative range histories are first grouped and subsequently partitioned by absolute slant range at each key pulse. For each resulting range subgroup, an actual scattering center within the subgroup is selected as the representative. The individual contributions are phase-calibrated to this representative and coherently summed to form an equivalent complex amplitude. At the associated non-key pulses, the stored amplitude is reused, while the representative supplies the current propagation delay and carrier phase. All other scattering-center contributions retain their individual form in Eq. (3). The sparse impulse response of the current pulse thus consists of equivalent entries and individually evaluated entries.

The remainder of this section develops the proposed method in four steps. Section 2.3.1 derives the propagation-phase deviation between an exact scattering-center contribution and

its representative-based approximation. Based on this deviation model, Section 2.3.2 forms the initial clusters and constrains their relative range-history variation. Section 2.3.3 then constructs the coherent equivalents at the key pulses and reuses their complex amplitudes at the associated non-key pulses. Finally, Section 2.3.4 assembles the equivalent and individually evaluated entries into the resulting sparse impulse response.

2.3.1 Unified Propagation-Phase Deviation Model

Consider a local set D containing several scattering centers, and select an actual scattering center q_D as the range and phase reference. Let k^* denote the reference key pulse at which the equivalent complex amplitude is formed. For the mth pulse and the nth scattering center in D, the propagation-induced spectral phase deviation between its exact frequency-domain contribution and the equivalent contribution represented by q_D is decomposed into an inter-pulse carrier-phase component and an intra-group baseband spectral-phase component as

$$\begin{aligned} \Delta\Psi_{n,D}(f,m;k^*) &= \Delta\Psi^c_{n,D}(m;k^*) + \Delta\Psi^b_{n,D}(f,m) \\ \Delta\Psi^c_{n,D}(m;k^*) &= \frac{4\pi}{\lambda}\left[(R_{n,m} - R_{q_D,m}) - (R_{n,k^*} - R_{q_D,k^*})\right] \\ \Delta\Psi^b_{n,D}(f,m) &= \frac{4\pi f}{c}(R_{n,m} - R_{q_D,m}), \end{aligned} \tag{5}$$

where $\Delta\Psi^c_{n,D}(m;k^*)$ denotes the inter-pulse carrier-phase deviation, and $\Delta\Psi^b_{n,D}(f,m)$ denotes the intra-group baseband spectral-phase deviation. The carrier-phase deviation is determined by the change in the scattering-center-to-reference relative range from the reference key pulse to the current pulse, and it becomes zero when $m = k^*$. The baseband spectral-phase deviation is determined by the instantaneous range separation between the scattering center and the reference one q_D, and it becomes zero at $f = 0$. Relative range-history constraints and the placement of key pulses control the carrier-phase deviation, while range grouping at key pulses and constraints control the baseband spectral-phase deviation. Coherence and visibility tests further determine whether the corresponding scattering-center contributions can be combined and reused.

2.3.2 Initial Grouping under Relative Range-History Constraints

Key pulses are selected approximately uniformly within each platform-state update interval. A sampled non-key pulse r_l and its nearest key pulse k_l in azimuth slow time form the lth range-history feature pair, where $l = 1,2,\dots,N_f$. The relative slant-range variation of the nth scattering center over this pair is

$$\Delta R_{n,l} = R_{n,r_l} - R_{n,k_l}. \tag{6}$$

Let the m_cth pulse be the aperture-center pulse. The unstandardized clustering feature vector of the nth scattering center is

$$\boldsymbol{z}_n = \left[\Delta R_{n,1} \quad \Delta R_{n,2} \quad \cdots \quad \Delta R_{n,N_f} \quad R_{n,m_c} \quad \boldsymbol{q}_n^{\mathrm{T}}\right]^{\mathrm{T}}. \tag{7}$$

The feature components are standardized to obtain the clustering input $\boldsymbol{f}_n$, whose component d is

$$\begin{cases} f_{n,d} = \frac{z_{n,d}-\mu_d}{\tilde{\sigma}_d}, \quad \tilde{\sigma}_d = \begin{cases} \sigma_d, & \sigma_d \geq \varepsilon_s \\ 1, & \sigma_d < \varepsilon_s \end{cases} \\ \mu_d = \frac{1}{N_s}\sum_{n=1}^{N_s} z_{n,d} \\ \sigma_d = \sqrt{\frac{1}{N_s-1}\sum_{n=1}^{N_s}(z_{n,d}-\mu_d)^2} \end{cases}, \tag{8}$$

where $f_{n,d}$ and $z_{n,d}$ are the standardized and unstandardized values of component d, respectively; N_s is the number of scattering centers; μ_d and σ_d are the sample mean and sample standard deviation of feature component d; $\tilde{\sigma}_d$ is the safeguarded standard deviation; and ε_s is double-precision machine epsilon, approximately 2.22×10^{-16}, used to avoid division by zero.

Within each partition defined by scattering mechanism and spatial location, K-medoids is applied to establish the initial groups. For the gth cluster G_g, the medoid index number is

$$q_g = \arg\min_{q \in G_g} \sum_{n \in G_g} \left\| \boldsymbol{f}_n - \boldsymbol{f}_q \right\|_2^2. \tag{9}$$

With N_{cl} denoting the total number of clusters, the clustering objective is

$$J = \sum_{g=1}^{N_{\mathrm{cl}}} \sum_{n \in G_g} \left\| \boldsymbol{f}_n - \boldsymbol{f}_{q_g} \right\|_2^2. \tag{10}$$

Equations (6)-(10) form parent clusters from scattering centers with similar relative range variations, scene ranges, and spatial positions. The range history of the actual medoid provides the reference for each parent cluster. Up to three non-key evaluation pulses are selected approximately uniformly from the slow-time interval associated with each key pulse. Each non-key evaluation pulse and its nearest key pulse form a range-history evaluation pair used to measure how the scattering-center-to-medoid range offset changes across the interval.

To assess range-history consistency of each candidate cluster, up to three non-key evaluation pulses are selected approximately uniformly from the azimuth-time interval associated with each key pulse, excluding the key pulse itself. The selected non-key evaluation pulse indexed by b and its reference key pulse form the bth range-history evaluation pair $(m_b, k_b), b = 1,2, \ldots, N_d$. For the bth range-history evaluation pair, the relative slant-range error of a cluster member with respect to its representative is

$$e_{n,g,b} = \left(R_{n,m_b} - R_{n,k_b}\right) - \left(R_{q_g,m_b} - R_{q_g,k_b}\right). \tag{11}$$

The root-mean-square (RMS) and maximum range-history errors of the parent cluster are defined as

$$\begin{cases} e_{\mathrm{RMS},g} = \sqrt{\frac{1}{N_g N_d} \sum_{b=1}^{N_d} \sum_{n \in G_g} e_{n,g,b}^2} \\ e_{\max,g} = \max |e_{n,g,b}| \end{cases}. \tag{12}$$

where $N_g = |G_g|$ is the number of scattering centers in the gth cluster G_g. The RMS statistic measures the overall dispersion of the scattering-center range histories relative to the cluster medoid. The maximum statistic records the largest scattering-center deviation in the parent cluster. A candidate cluster must satisfy both $e_{\mathrm{RMS},g} \le \varepsilon_{\mathrm{RMS}}$ and $e_{max,g} \le \varepsilon_{max}$, where $\varepsilon_{\mathrm{RMS}}$ and ε_{max} are the RMS and maximum range-history error thresholds, respectively. The main experiments use refinement thresholds of 0.10 mm and 0.40 mm, respectively. A one-way range-history residual produces the following two-way carrier-phase perturbation:

$$\Delta\Phi = \frac{4\pi e_{n,g,b}}{\lambda}. \tag{13}$$

Equations (11)-(13) convert the relative range-history differences within a parent cluster into measurable range and carrier-phase quantities. When either statistic exceeds its threshold and further splitting is permitted, the parent cluster is bisected along the feature component with the largest dispersion. The cluster medoid and error statistics are then recomputed. Refinement continues until both statistics satisfy their thresholds or the prescribed minimum cluster size or maximum number of splits is reached. The refined parent clusters are passed to range grouping at key pulses. The next subsection evaluates the slant-range extent and coherent summation of each resulting range subgroup before constructing an equivalent entry.

2.3.3 Coherent Equivalence at Key Pulses and Inter-Pulse Reuse

The initial grouping places scattering centers with similar relative range histories in the same parent cluster. At each key pulse, the visible scattering centers in every parent cluster are divided by absolute slant range into range subgroups. Each range subgroup therefore contains visible scattering centers from one parent cluster whose delays occupy a limited interval. Phase calibration and coherent summation are performed within that interval.

For a range subgroup D formed at the kth key pulse, the amplitude-weighted mean slant range is

$$\overline{R}_{D,k} = \sum_{n\in D} \frac{|a_{n,k}|}{\sum_{i\in D}|a_{i,k}|} R_{n,k}. \tag{14}$$

The scattering center whose slant range is closest to the amplitude-weighted mean range is selected as the representative:

$$q_D = \arg\min_{n\in D} |R_{n,k} - \overline{R}_{D,k}|. \tag{15}$$

For the nth scattering center in D, the carrier-phase calibration factor and the equivalent complex amplitude at the key pulse are

$$\gamma_{n,k}^{D} = \exp\left[-j\frac{4\pi}{\lambda}(R_{n,k} - R_{q_D,k})\right], \tag{16}$$

$$A_{D,k} = \sum_{n\in D} a_{n,k}\, \gamma_{n,k}^{D}. \tag{17}$$

Equation (16) transfers the carrier phase of every scattering center in the range subgroup to the phase reference of its selected representative. Equation (17) then sums the calibrated contributions of all visible scattering centers in that range subgroup to obtain the equivalent complex amplitude. At the key pulse, the inter-pulse carrier-phase component in Eq. (5) equals zero. The instantaneous delay support and the stability of coherent summation therefore determine whether the range subgroup can be represented by one sparse-response entry.

For range subgroup D at the kth key pulse, the slant-range span, amplitude-weighted range standard deviation, and coherence ratio are used to characterize the worst-case range extent, the range concentration of the dominant scattering energy, and the stability of coherent summation, respectively:

$$W_{D,k} = \max_{n\in D} R_{n,k} - \min_{n\in D} R_{n,k}, \tag{18}$$

$$\sigma_{D,k} = \sqrt{\sum_{n\in D} \frac{|a_{n,k}|}{\sum_{i\in D}|a_{i,k}|}(R_{n,k} - \overline{R}_{D,k})^2}, \tag{19}$$

$$\rho_{D,k} = \frac{|A_{D,k}|}{\max(\sum_{n\in D}|a_{n,k}|, \varepsilon_s)}. \tag{20}$$

The range span in Eq. (18) limits the maximum delay interval covered by one equivalent entry. The weighted standard deviation in Eq. (19) measures the concentration of the dominant scattering energy within that interval. The coherence ratio in Eq. (20) compares the magnitude retained after coherent summation with the sum of the individual scattering-center magnitudes. A range subgroup is accepted as a local coherent equivalent if

$$\begin{cases} W_{D,k} \le W_{\max} \\ \sigma_{D,k} \le \sigma_{\max} \\ \rho_{D,k} \ge \rho_{\min} \end{cases}, \tag{21}$$

where W_{max}, σ_{max} , and ρ_{min} are the thresholds for the slant-range span, amplitude-weighted range standard deviation, and coherence ratio, respectively. They are set to 0.125 m, 0.036 m, and 0.035 in the experiments.

For each range subgroup satisfying Eq. (21), its representative q_D and equivalent complex amplitude A_{D,k^*} are retained for use within the pulse interval referenced to k^* . At the current pulse, the complex amplitude is reused, while the propagation delay and carrier phase of the response entry are updated using the current slant range of q_D.

If the current pulse is itself a key pulse, $k^* = m$; otherwise, k^* denotes its reference key pulse. An amplitude-scaling factor is introduced to account for the change in the representative-point complex amplitude from k^* to m .

For range subgroup D , the amplitude-scaling factor is defined as

$$\beta_{D,m,k^*} = \frac{|a_{q_D,m}|}{\max(|a_{q_D,k^*}|, \varepsilon_s)}. \tag{22}$$

At the reference key pulse, $\beta_{D,m,k^*} = 1$ when the magnitude of the representative-point coefficient is nonzero. Combining the equivalent complex amplitude, amplitude scaling, and the current representative-point geometry gives the equivalent sparse-response contribution of D at the current pulse:

$$h_{D,m}(\tau) = \beta_{D,m,k^*} A_{D,k^*} \exp\left(-j\frac{4\pi R_{q_D,m}}{\lambda}\right) \delta\left(\tau - \frac{2R_{q_D,m}}{c}\right). \tag{23}$$

In Eq. (23), the equivalent complex amplitude at the key pulse retains the coherently summed scattering-center contributions. The amplitude-scaling factor corrects the change in the representative complex-amplitude magnitude from the key pulse to the current pulse, and the current representative slant range supplies the propagation delay and carrier phase. The scattering-center contributions in the range subgroup are therefore combined once at the key pulse and subsequently represented by one entry whose geometry follows the selected representative.

At the current pulse, an accepted range subgroup contributes through Eq. (23) when its selected representative is visible from the current observation direction and its complex amplitude is valid. Scattering centers outside the accepted range subgroups are evaluated individually. The same individual evaluation is used when an accepted subgroup cannot provide a valid equivalent entry at the current pulse. Each individually evaluated scattering center contributes through Eq. (3).

2.3.4 Equivalent Sparse Impulse Response

Let L_m denote the range subgroups that provide valid equivalent entries through Eq. (23) at the current pulse. Let I_m^{dir} denote the visible scattering centers evaluated individually through Eq. (3). Each range subgroup in L_m contributes one equivalent entry, and every scattering center in I_m^{dir} retains its individual contribution. The resulting equivalent sparse impulse response is

$$h_m(\tau) = \sum_{D\in L_m} h_{D,m}(\tau) + \sum_{n\in I_m^{\mathrm{dir}}} a_{n,m} \exp\left(-j\frac{4\pi R_{n,m}}{\lambda}\right) \delta\left(\tau - \frac{2R_{n,m}}{c}\right) \tag{24}$$

Equation (24) combines the range-subgroup equivalents and the individually evaluated scattering-center terms for the current pulse. A range subgroup containing several scattering centers contributes one equivalent entry. Scattering centers that do not satisfy the equivalence conditions retain their original entries. The response construction therefore generates the equivalent entries of accepted range subgroups and the individual entries of the remaining scattering centers. This representation reduces the number of complex-amplitude updates at non-key pulses and the number of sparse entries processed before frequency-domain convolution. Substituting Eq. (24) into Eq. (4) yields the raw echo for the current pulse.

3 Experimental Setup

3.1 Comparison Methods and Common Scene

Baseline A serves as the direct time-domain numerical reference. Baseline B uses the full sparse impulse response in Eq. (3), while the proposed method uses the locally equivalent response in Eq. (24); both then follow the same frequency-domain echo-synthesis procedure. All methods use the same target representation and pulsewise trajectories under the parameters in Table 1.

Evaluation begins with a straight-line broadside trajectory (M0), followed by three nonuniform trajectories (M1–M3) and a 15° forward-squint acquisition combined with M3. Ablations isolate inter-pulse reuse (C1) and spatial aggregation (C2), while sensitivity studies vary the number of key pulses and the RMS relative range-history threshold.

Table 1 Common monostatic spotlight SAR and target-scene parameters.

Parameter	Symbol	Value
Carrier frequency	f_c	10 GHz
Signal bandwidth	B	480 MHz
Pulse duration	T_p	5 μs
Sampling frequency	f_s	1.152 GHz
Pulse repetition frequency	PRF	10 kHz
Synthetic aperture duration	T_{op}	0.85 s
Nominal platform speed	v_0	250 m/s
Platform altitude	H	5000 m
Ground range at aperture center	R_g	8000 m

3.2 Scattering-Center Selection and Algorithm Parameters

The experiments use a three-dimensional ship model with a prescribed waterline. The fixed scattering-center library is constructed using three categories: prominent-edge centers on selected hull and structural edges, facet-surface centers on above-water hull and superstructure facets, and waterline/dihedral centers near the waterline and hull sides. All methods use the same 28,115-center library and pulse-dependent visibility and aspect-response model. Figure 2 shows the target geometry and the three scattering-center categories.

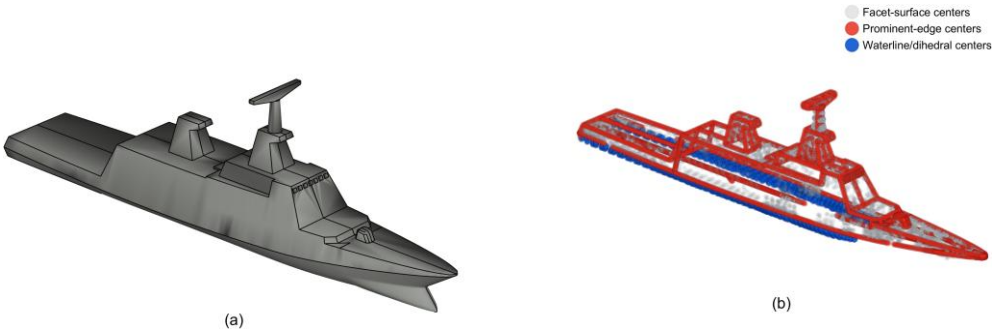


Fig. 2 Ship-target representation. (a) Three-dimensional geometry; (b) three scattering-center categories.

With the target representation held fixed, the proposed method is evaluated using the parameter settings in Table 2.

Table 2 Principal parameters of the proposed method.

Parameter	Symbol	Value
Platform-state update interval	T_u	25 ms
Number of key pulses per update interval	N_{kp}	3
RMS range-history error limit	$\varepsilon_{\mathrm{RMS}}$	0.10 mm
Maximum range-history error limit	ε_{max}	0.40 mm
Initial target cluster size	--	14 scattering centers
Range-bin width key pulses	--	0.095 m
Maximum subgroup range span	W_{max}	0.125 m
Maximum weighted range standard deviation	σ_{max}	0.036 m
Minimum coherence ratio	ρ_{min}	0.035
Amplitude scale interval	η_{min}, η_{max}	0.55,1.90
Local explicit-selection percentile	--	97%
Explicit-center limits	--	2–35 per partition; 1000 overall

3.3 Evaluation Metrics

All simulated raw echoes undergo the same matched-filter range compression and back-projection (BP) imaging [18]. We assess acceleration and the fidelity of the simulated echoes and BP images, while also examining the compactness of the equivalent sparse response. Acceleration is expressed as speedup, defined as the online runtime of Baseline B divided by that of the evaluated method. Fidelity is assessed using the normalized root-mean-square error (NRMSE) of the complex echo array S_X and BP image array M_X :

$$\begin{cases} \mathrm{NRMSE}_{\mathrm{echo}} = \dfrac{\|S_X - S_{\mathrm{A}}\|_F}{\|S_{\mathrm{A}}\|_F} \\ \mathrm{NRMSE}_{\mathrm{BP}} = \dfrac{\|M_X - M_{\mathrm{A}}\|_F}{\|M_{\mathrm{A}}\|_F} \end{cases}, \quad X \in \{\mathrm{B}, \mathrm{C}\}. \tag{25}$$

The effective-entry compression ratio, which exceeds one when equivalence reduces the number of sparse-response entries, is defined as

$$\varsigma_c = \frac{\sum_m |I_m|}{\sum_m |L_m| + \sum_m |I_m^{dir}|}, \tag{26}$$

4 Results and Discussion

This section evaluates the fidelity and online efficiency of the proposed method (C) across the tested geometries, examines the contributions of spatial aggregation and inter-pulse reuse, and studies the fidelity–efficiency trade-off of two control parameters. Baseline A is the direct time-domain reference. Baseline B uses the same frequency-domain synthesis backend as C without local coherent equivalence. Complex raw-echo and back-projection (BP) image NRMSE are evaluated separately against A for each case.

4.1 Performance across trajectories and squint angles

Figure 3 compares the M0 BP images of A, B, and C on a common amplitude scale. B closely reproduces A, whereas C retains the principal ship structure and bright-scatterer locations but has about 4.5 times the raw-echo error and 12.3 times the BP error of B (Table 3). The common-scale images show that dominant structure remains visible; they do not establish an application-specific tolerance for the larger complex errors.

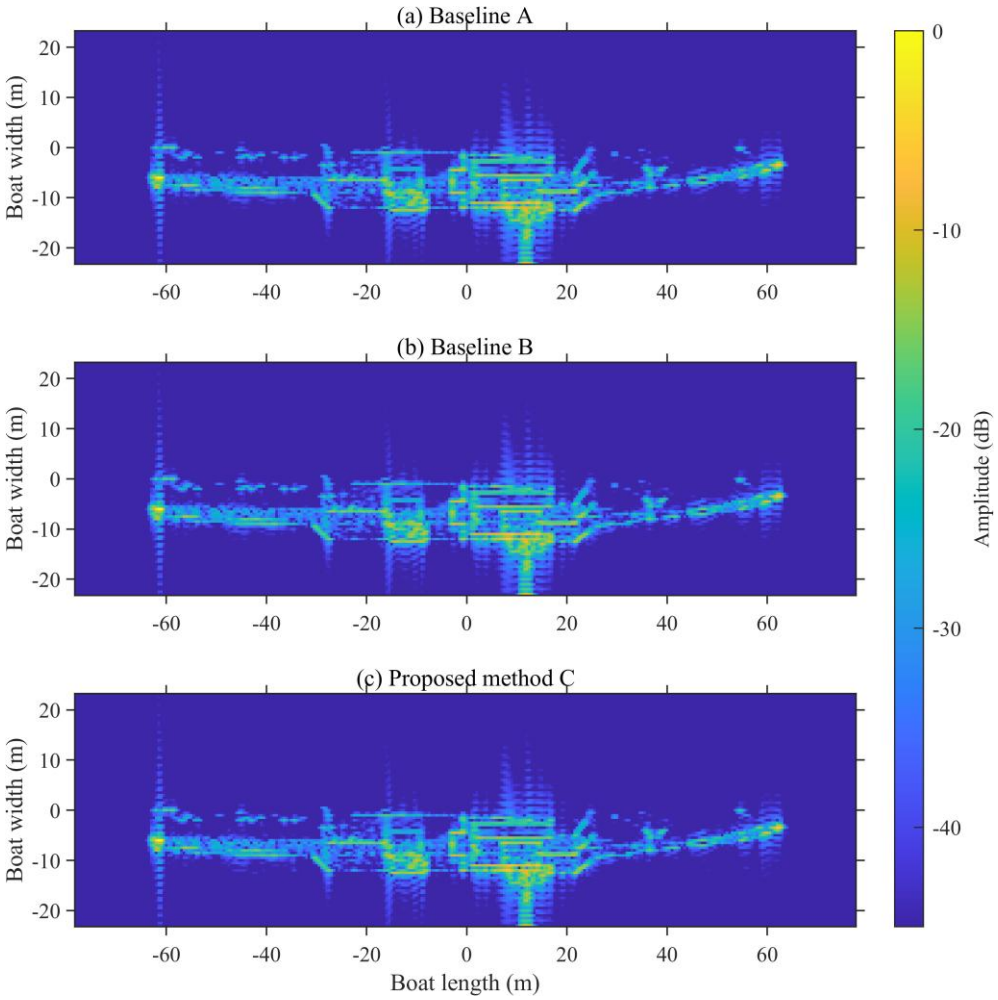


Fig. 3 BP images for M0. (a) Direct time-domain Baseline A; (b) frequency-domain Baseline B; (c) proposed method C. All panels use the same A-reference peak, color scale, and physical coordinates.

Table 3 quantifies this trade-off across the four broadside trajectories. C reduces median online generation time from approximately 350 s for B to 114–116 s per case, yielding speedups of 3.028–3.114. Across M0–M3, C's complex raw-echo and BP NRMSE remain near 0.061 and 0.053, compared with about 0.0135 and 0.0043 for B. The speedup declines monotonically from 3.114 (M0) to 3.028 (M3), a spread of only 2.8%, and the four trajectories do not isolate trajectory complexity as its cause.

The effective-entry compression ratio of C is lower than its online speedup in every case (Table 3). Spatial aggregation reduces the number of response entries, and inter-pulse reuse reduces how often equivalent responses are rebuilt. Validity checks, pointwise contributions, sparse gridding, and FFT synthesis still consume online time, so the entry ratio alone cannot predict the speedup.

Table 3 Fidelity and online generation across the four broadside trajectories.

Case	Method	Raw-echo NRMSE	BP NRMSE	Effective-entry compression ratio	Online time(s)	Online speedup over B
M0	B	0.013531	0.004272	1.0000	354.34	1.000
	C	0.060682	0.052579	1.7755	113.78	3.114
M1	B	0.013538	0.004296	1.0000	352.15	1.000
	C	0.060665	0.052615	1.7753	113.57	3.101
M2	B	0.013535	0.004280	1.0000	349.82	1.000
	C	0.060681	0.052583	1.7741	114.99	3.042
M3	B	0.013526	0.004286	1.0000	350.40	1.000
	C	0.060635	0.052612	1.7746	115.73	3.028

Note:NRMSE is relative to same-case A. Effective-entry compression compares the uncompressed visible-center entries of B with the equivalent subgroup plus pointwise entries of C. Times are medians of six online runs; speedup is median(B) / median(C). Offline plan construction, disk I/O, range compression, and BP imaging are excluded.

Across six repeated runs in each of the five tested cases, the coefficients of variation of B and C online times range from 4.8% to 9.2% and from 4.0% to 6.7%, respectively, and all 30 within-round B/C time ratios exceed 2.56. These repetitions assess timing variation for the same deterministic cases, not variation across independent targets or trajectories.

For M3 at 15° forward squint, C gives raw-echo and BP NRMSE of 0.044007 and 0.038082 and a 2.719-fold speedup (B median 369.32 s, C median 135.84 s), with the effective-entry compression ratio falling to 1.5494. The lower compression and speedup than for broadside M3 suggest that altered range projection, visibility, and aspect response affect the opportunities for accepted equivalence. The lower NRMSE does not establish that squint is intrinsically easier, because each acquisition case has its own A reference and only one squint angle was tested.

4.2 Module ablation

Figure 4 compares B with inter-pulse reuse only (C1), spatial aggregation only (C2), and the complete method C for M0 and M3. C1 keeps the effective-entry count unchanged and has essentially the same raw-echo NRMSE as B (Fig. 4(b)), with online speedups of 0.943 (M0) and 0.941 (M3). Inter-pulse reuse alone therefore provides no independent online gain in this implementation.

C2 achieves an effective-entry compression ratio of about 2.46 relative to B, yet its online speedups are only 0.144 (M0) and 0.143 (M3), approximately seven times slower than B. Equivalent-response rebuilding and updating at every pulse account for about 93.3% of its online time, outweighing the savings from fewer entries; this outcome reflects the tested implementation and timing scope. C2 also has a larger raw-echo NRMSE (about 0.0845); the C2–C comparison does not hold accepted groups or representative points fixed, so the error difference cannot be attributed to entry compression alone.

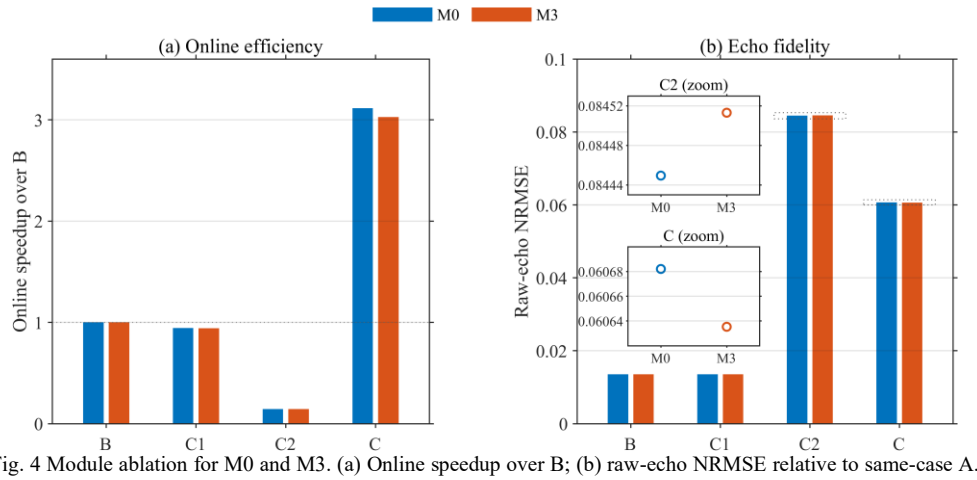


Fig. 4 Module ablation for M0 and M3. (a) Online speedup over B; (b) raw-echo NRMSE relative to same-case A. C1 uses inter-pulse reuse only, C2 spatial aggregation only, and C combines both.

Complete C combines fewer sparse-response entries with less frequent reconstruction of the equivalent complex response, and it is the only tested acceleration variant that is faster than

B; its speedups and errors are those of the main configuration in Table 3. The small M0–M3 NRMSE differences in the enlarged views do not establish a trajectory effect.

4.3 Parameter sensitivity

Figure 5 shows the effects of varying the number of key pulses per 25-ms update interval and the RMS relative range-history subdivision threshold. The first sweep uses 1, 2, 3, 5, and 7 key pulses; the second spans 0.05–1.00 mm, with the threshold on the maximum relative range-history deviation set to four times each RMS value (0.40 mm at the selected 0.10 mm setting).

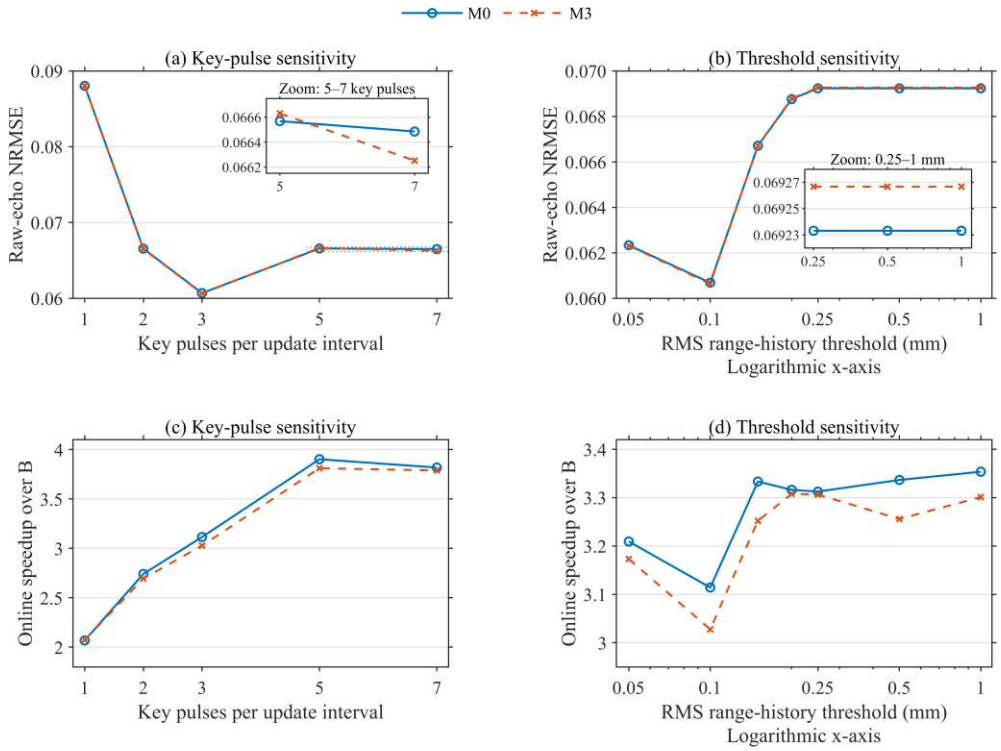


Fig. 5 Parameter sensitivity for M0 and M3. Left: key pulses per 25-ms interval; right: RMS range-history threshold. Top: raw-echo NRMSE relative to same-case A; bottom: online speedup over same-case B.

Increasing the key-pulse count from one to three lowers raw-echo NRMSE from about 0.088 to 0.061 for both trajectories and raises online speedup from about 2.07 to 3.03–3.11.

At five pulses, speedup rises to 3.901 and 3.810, but raw-echo NRMSE also rises to 0.066569 and 0.066630 for M0 and M3, respectively. Thus, the three-pulse setting used in Sections 4.1 and 4.2 favors fidelity, while five pulses favor online efficiency.

At seven pulses, raw-echo NRMSE decreases slightly from the five-pulse values to 0.066486 for M0 and 0.066252 for M3, while speedup decreases to 3.817 and 3.788; seven pulses therefore offer a small error reduction at a slightly lower measured speedup. Key-pulse layout also changes range-history features, clusters, and representative points, so the sweep does not isolate temporal sampling density at fixed spatial grouping or imply a monotonic error trend.

The 0.10 mm threshold gives the lowest measured raw-echo NRMSE but also the lowest median speedups in the threshold sweep—3.114 for M0 and 3.028 for M3—as shown in Fig. 5(b) and Fig. 5(d). At 0.05 mm, speedups are 3.209 and 3.173, but clustering reaches the 4200-cluster limit, so this point does not isolate the effect of a tighter accepted error bound. Raising the threshold to 0.15 mm increases raw-echo NRMSE to about 0.0667; at 0.25 mm raw-echo NRMSE reaches 0.069233 and 0.069267, while speedup is about 3.31 in both cases. The 0.25, 0.50, and 1.00 mm points produce identical raw echoes and fidelity values; small timing differences should be interpreted cautiously in view of run-to-run variation.

The selected three-pulse, 0.10 mm setting is a fidelity-first point on the tested parameter grid, not a joint optimum for error and online time. The 0.10 mm value is a subdivision target subject to minimum cluster size and other termination conditions, rather than a guaranteed upper bound on every final parent cluster.

4.4 Discussion and scope

Overall, C trades a measured increase in complex echo and BP error for an approximately threefold reduction in online generation time across the four broadside cases; the single 15° forward-squint case yields a 2.719-fold speedup over B. Among the tested ablation variants, only the combination of spatial aggregation and inter-pulse reuse is faster than B. In the

tested parameter grid, three key pulses and a 0.10 mm RMS threshold favor fidelity, while five key pulses or several thresholds above 0.10 mm yield higher measured speedups at higher raw-echo error.

Xie et al. [16] use equidistant rings and polar subscenes to calculate transfer functions jointly for pulses in a subaperture under arbitrary motion. Their later one-stationary bistatic method [17] uses equidistant elliptical rings and subscene processing while accounting for moving-platform motion errors. In contrast, C locally groups a prebuilt three-dimensional scattering-center library and reuses equivalent complex responses assigned to key pulses, while updating the representative-point delay and carrier phase and checking visibility at each pulse. The speedup factors reported in [16, 17] cannot be compared directly with those in Table 3 because the targets, geometries, and timing scopes differ.

These findings apply to a single prebuilt ship scattering-center library, smooth physically bounded trajectories, one tested forward-squint angle, and the central processing unit (CPU) implementation. Offline plan construction, disk I/O, range compression, and BP imaging are outside the reported online timing; end-to-end speedup and behavior under stronger local motion, other targets, and more squint angles remain to be established.

5 Conclusions

This study developed an error-constrained local coherent equivalence method for fast spotlight SAR raw data generation. A unified propagation-phase model distinguishes the inter-pulse carrier-phase deviation introduced by key-pulse reuse from the baseband spectral-phase deviation introduced by replacing multiple scattering-center delays with one representative delay. Relative range-history grouping, range-support and coherence criteria, visibility checks, amplitude updates, and pointwise fallback govern the equivalent sparse response.

Across M0–M3, the complete method achieved 3.028–3.114-fold online speedups over Baseline B. Its complex raw-echo and BP-image NRMSEs relative to the same-case

Baseline A were approximately 0.061 and 0.053, compared with about 0.0135 and 0.0043 for B. In the single M3 acquisition at 15° forward squint, it achieved a 2.719-fold speedup, with raw-echo and BP-image NRMSEs of 0.044007 and 0.038082.

Among the tested ablation variants, only the combination of spatial aggregation and inter-pulse reuse was faster than B. Three key pulses and a 0.10 mm RMS threshold favored fidelity on the tested parameter grid; five key pulses or several larger thresholds produced higher measured speedups at higher raw-echo error. These findings are limited to the tested ship library, geometries, and CPU implementation. Offline plan construction, disk I/O, range compression, and BP imaging are excluded from the reported online timing.

List of abbreviations

SAR, synthetic aperture radar; BP, back projection; FFT, fast Fourier transform; NRMSE, normalized root-mean-square error; RMS, root-mean-square; CPU, central processing unit; PRF, pulse repetition frequency.

Declarations

Availability of data and materials

The datasets used and/or analyzed during the current study are available from the corresponding author on reasonable request.

Competing interests

The authors declare that they have no competing interests.

Funding

This research received no funding.

Authors' contributions

Conceptualization: J.L. and L.Z.; methodology: J.L. and L.Z.; software: J.L.; validation: J.L. and X.C.; formal analysis: J.L. and L.Z.; investigation: T.J.; resources: C.L. and S.Z.; data curation: J.L.; writing—original draft preparation: J.L.; writing—review and editing: L.Z., C.L., and S.Z.; visualization: J.L.; supervision: L.Z., C.L., and S.Z.; project administration: X.C. and T.J.

Acknowledgements

Not applicable.

References

[1] G. Franceschetti, M. Migliaccio, D. Riccio, G. Schirinzi, SARAS: A synthetic aperture radar (SAR) raw signal simulator. IEEE Trans. Geosci. Remote Sens. 30, 110–123 (1992). https://doi.org/10.1109/36.124221

[2] S. Cimmino, G. Franceschetti, A. Iodice, D. Riccio, G. Ruello, Efficient spotlight SAR raw signal simulation of extended scenes. IEEE Trans. Geosci. Remote Sens. 41, 2329–2337 (2003). https://doi.org/10.1109/TGRS.2003.815239

[3] D.A.G. Dell'Aglio, G. Di Martino, A. Iodice, D. Riccio, G. Ruello, A unified formulation of SAR raw signals from extended scenes for all acquisition modes with application to simulation. IEEE Trans. Geosci. Remote Sens. 56, 4956–4967 (2018). https://doi.org/10.1109/TGRS.2018.2844094

[4] A. Mori, F. De Vita, A time-domain raw signal simulator for interferometric SAR. IEEE Trans. Geosci. Remote Sens. 42, 1811–1817 (2004). https://doi.org/10.1109/TGRS.2004.832242

[5] H. Lee, K.W. Kim, An integrated raw data simulator for airborne spotlight ECCM SAR. Remote Sens. 14, 3897 (2022). https://doi.org/10.3390/rs14163897

[6] O. Dogan, M. Kartal, Time Domain SAR Raw Data Simulation of Distributed Targets. EURASIP J. Adv. Signal Process. 2010, 784815 (2010). https://doi.org/10.1155/2010/784815

[7] G. Franceschetti, A. Iodice, S. Perna, D. Riccio, SAR sensor trajectory deviations: Fourier domain formulation and extended scene simulation of raw signal. IEEE Trans. Geosci. Remote Sens. 44, 2323–2334 (2006). https://doi.org/10.1109/TGRS.2006.873206

[8] Z. Guo, Z. Fu, J. Chang, L. Wu, N. Li, A novel high-squint spotlight SAR raw data simulation scheme in 2-D frequency domain. Remote Sens. 14, 651 (2022). https://doi.org/10.3390/rs14030651

[9] Y. Huai, Y. Liang, J. Ding, M. Xing, L. Zeng, Z. Li, An inverse extended Omega-K algorithm for SAR raw data simulation with trajectory deviations. IEEE Geosci. Remote Sens. Lett. 13, 826–830 (2016). https://doi.org/10.1109/LGRS.2016.2548240

[10] Y. Liu, W. Wang, X. Pan, Z. Gu, G. Wang, Raw signal simulator for SAR with trajectory deviation based on spatial spectrum analysis. IEEE Trans. Geosci. Remote Sens. 55, 6651–6665 (2017). https://doi.org/10.1109/TGRS.2017.2731364

[11] S. Dai, H. Zhang, C. Wang, Z. Lin, Y. Zhang, J. Ran, An efficient SAR raw signal simulator accounting for large trajectory deviation. Sensors 25, 4260 (2025). https://doi.org/10.3390/s25144260

[12] B. Wan, L. Zhang, J. Wu, G. Wang, Z. Xi, An efficient hybrid domain algorithm for accurate SAR raw data generation with trajectory deviations. IEEE Geosci. Remote Sens. Lett. 22, 1–5 (2025). https://doi.org/10.1109/LGRS.2025.3528935. Article 4005105

[13] S. Zhang, W. Zhang, L. Kong, SAR raw signal simulation based on sub-aperture processing, in Proceedings of the 2010 IEEE Radar Conference (Washington, DC, USA, 2010), pp. 569–572. https://doi.org/10.1109/RADAR.2010.5494555

564 [14] L. Wen, T. Zeng, A sub-aperture-based SAR raw signal generation method, in IET
565 International Radar Conference (2009), pp. 146–149.
566 https://doi.org/10.1049/cp.2009.0125
567 [15] R. Sofiani, H. Heidar, M. Kazerooni, An efficient raw data simulation algorithm for
568 large complex marine targets and extended sea clutter in spotlight SAR. Microw. Opt.
569 Technol. Lett. 60, 1223–1230 (2018). https://doi.org/10.1002/mop.31143
570 [16] H.T. Xie, D.X. An, X.T. Huang, Z.M. Zhou, Efficient raw signal generation based on
571 equivalent scatterer and subaperture processing for SAR with arbitrary motion.
572 Radioengineering 23, 1169–1179 (2014)
573 [17] H.T. Xie, D.X. An, X.T. Huang, Z.M. Zhou, Efficient raw signal generation based on
574 equivalent scatterer and subaperture processing for one-stationary bistatic SAR
575 including motion errors. IEEE Trans. Geosci. Remote Sens. 54, 3360–3377 (2016).
576 https://doi.org/10.1109/TGRS.2016.2516046
577 [18] H. Cruz, M. Véstias, J. Monteiro, H. Neto, R.P. Duarte, A review of synthetic-aperture
578 radar image formation algorithms and implementations: A computational perspective.
579 Remote Sens. 14, 1258 (2022). https://doi.org/10.3390/rs14051258